

On the synthesis of morphology-controlled transition metal dichalcogenides via chemical vapor deposition for electrochemical hydrogen generation

Sharma, Rahul; Sahoo, Krishna Rani; Rastogi, Pankaj Kumar; Biroju, Ravi K.; Theis, Wolfgang; Narayanan, Tharangattu N.

DOI:

[10.1002/pssr.201900257](https://doi.org/10.1002/pssr.201900257)

License:

None: All rights reserved

Document Version

Peer reviewed version

Citation for published version (Harvard):

Sharma, R, Sahoo, KR, Rastogi, PK, Biroju, RK, Theis, W & Narayanan, TN 2019, 'On the synthesis of morphology-controlled transition metal dichalcogenides via chemical vapor deposition for electrochemical hydrogen generation', *Physica Status Solidi - Rapid Research Letters*, vol. 13, no. 12, 1900257, pp. 1-10. <https://doi.org/10.1002/pssr.201900257>

[Link to publication on Research at Birmingham portal](#)

Publisher Rights Statement:

Checked for eligibility: 05/07/2019

This is the peer reviewed version of the following article: Sharma, R. , Sahoo, K. R., Rastogi, P. K., Biroju, R. K., Theis, W. and Narayanan, T. N. (2019), On the Synthesis of Morphology Controlled Transition Metal Dichalcogenides via CVD for Electrochemical Hydrogen Generation. *Phys. Status Solidi RRL*. doi:10.1002/pssr.201900257, which has been published in final form at doi:10.1002/pssr.201900257. This article may be used for non-commercial purposes in accordance with Wiley Terms and Conditions for Use of Self-Archived Versions.

General rights

Unless a licence is specified above, all rights (including copyright and moral rights) in this document are retained by the authors and/or the copyright holders. The express permission of the copyright holder must be obtained for any use of this material other than for purposes permitted by law.

- Users may freely distribute the URL that is used to identify this publication.
- Users may download and/or print one copy of the publication from the University of Birmingham research portal for the purpose of private study or non-commercial research.
- User may use extracts from the document in line with the concept of 'fair dealing' under the Copyright, Designs and Patents Act 1988 (?)
- Users may not further distribute the material nor use it for the purposes of commercial gain.

Where a licence is displayed above, please note the terms and conditions of the licence govern your use of this document.

When citing, please reference the published version.

Take down policy

While the University of Birmingham exercises care and attention in making items available there are rare occasions when an item has been uploaded in error or has been deemed to be commercially or otherwise sensitive.

If you believe that this is the case for this document, please contact UBIRA@lists.bham.ac.uk providing details and we will remove access to the work immediately and investigate.

On the Synthesis of Morphology Controlled Transition Metal Dichalcogenides via CVD for Electrochemical Hydrogen Generation

Rahul Sharma[#], Krishna Rani Sahoo^{#1}, Pankaj Kumar Rastogi[#], Ravi K. Biroju[#], Wolfgang Theis, and Tharangattu N. Narayanan^{*1}

Rahul Sharma, Krishna Rani Sahoo, Dr. Pankaj Kumar Rastogi, and Dr. Tharangattu N. Narayanan

Tata Institute of Fundamental Research - Hyderabad, Sy. No. 36/P, Serilingampally Mandal, Gopanapally Village, Hyderabad - 500 107, India.

E-mail: tn_narayanan@yahoo.com or tnn@tifrh.res.in.

Dr. Ravi K. Biroju and Dr. Wolfgang Theis

Nanoscale Physics Research Laboratory, School of Physics and Astronomy, University of Birmingham, Birmingham B15 2TT, UK.

[#] *Equally contributing authors.*

Keywords: CVD, Transition Metal Dichalcogenide, Dendritic Structures, Hydrogen Evolution, Atomically Thin Alloys.

This article has been accepted for publication and undergone full peer review but has not been through the copyediting, typesetting, pagination and proofreading process, which may lead to differences between this version and the [Version of Record](#). Please cite this article as doi: [10.1002/pssr.201900257](https://doi.org/10.1002/pssr.201900257)

This article is protected by copyright. All rights reserved

Abstract

Shape engineered atomically thin transition metal dichalcogenide (TMD) crystals are highly intriguing systems in regards to both fundamental and applied science. Here, a chemical vapour deposition assisted generalized synthesis strategy for the triangular and dendritic shaped TMDs and their ternary alloys is proposed, and the TMD structures' potential for electrocatalytic hydrogen evolution reaction (HER) applications is demonstrated. The alloy formation is confirmed *via* micro-Raman and photoluminescence studies, and further verified by transmission electron microscopy and X-ray photoelectron spectroscopy. The HER activities of MoS₂ and MoSe₂ triangles are compared with those of their dendritic structures, and an enormous improvement in terms of overpotential and current density is observed for the dendritic structures. A further enhancement of the HER activity is observed in MoS_{2(1-x)}Se_{2x} triangular and dendritic structures, with dendritic MoS_{2(1-x)}Se_{2x} providing the best activity. The demonstrated non-equilibrium growth technique opens new avenues for the synthesis of morphology controlled, large area, complex, atomically thin TMD structures, which can have unprecedented properties such as the enormous catalytic activity, tunable luminescence etc., as presented here.

Engineering the structure and morphology of atomically thin layers (two dimensional/2D materials) is receiving tremendous attention due to both fundamental and applied interest.^[1] The quantum confinement effects can yield drastic and unprecedented changes in the physical properties of 2D layers.^[2] It is found that the nature and the position of Dirac cone in graphene,^[3] the indirect to direct band gap transition,^[4] and the spin orbit coupling of transition metal dichalcogenides (TMDs)^[5] are tunable by controlling the morphology. Through this, structure and morphology control of TMDs can have high impact on their electronic,^[6] optical,^[7] and photo-/electrocatalytic properties.^[8] Hence, methods for the controlled growth of complex TMD structures are in high demand.^[9]

Several self-organized patterns of atomic layers were reported in the recent past, including structures such as snowflake-like graphene structures,^[10] dendritic graphene^[11] and TMD structures,^[8] polygons of TMDs^[12] and their alloys.^[13] Growing these complex structures of micrometer length scales in a controllable and uniform fashion is rather challenging.^[10, 14] Developing their ternary, quaternary, or higher order mixtures having different metal/chalcogen dopants in order to engineer their physical properties is an active area of research.^[15] Top-down growth methods such as liquid exfoliation,^[16] mechanical exfoliation^[17] etc. are not viable for the morphology controlled 2D material synthesis since most of these engineered structures are only form under non-equilibrium growth conditions. The chemical vapour deposition (CVD) technique is ideal for such morphology controlled structures since the growth process in this case can be tuned both kinetically and thermodynamically by controlling the pressure temperature profile.^[11-12]

TMDs, especially MoS₂, are well researched for their catalytic activity, particularly for their electro-/photo-electro catalytic hydrogen generation (HER).^[18] Though thermodynamically

many TMDs favor HER ($\Delta G_H \sim 0\text{eV}$),^[19] their catalytic activity is limited kinetically due to the basal plane's inactivity.^[20] To circumvent this issue, either the basal plane has to be made active or more edge exposure needs to be achieved for enhancing the exchange current density.^[8, 20] The development of size confined structures such as quantum dots is an approach to make large edge exposed TMDs, but the chemical techniques employed to generate such confined structures result in oxidized edge states, hence hamper the charge transfer properties.^[21] On the other hand, Wenshuo Xu *et al.* have recently reported a CVD based growth technique for dendritic MoS₂ structures, exhibiting an enhanced number of edge sites.^[22] They controlled the Mo/S vapour concentration by varying the height of the Si/SiO₂ substrate in the CVD chamber and demonstrated that a low concentration of Mo/S vapors gives rise to dendritic structures. Further, it was also found that the dendritic structures of TMDs have higher HER electro-catalytic activity than their triangular structures (the most common polygon shape obtained during monolayer MoS₂ growth) because of the presence of enhanced number of edge sites in these structures. Similarly, dendritic MoS₂ structures can also be generated by varying the growth temperature, where it is found that MoS₂ flakes can vary from highly fractal to relatively compact as the growth temperature varies from low to high (730 °C to 880 °C). It is believed that higher growth temperatures enhance the surface migration of precursors and the crystallization of MoS₂ flakes, thus yielding more compact structures.^[23]

Along with the edge plane electrocatalytic activity of TMDs, there are both theoretical and experimental reports on the tunability of the basal plane's activity of TMDs by forming their ternary or quaternary alloys (in-plane mixtures of different metals and/or chalcogens in different ratios)^[13, 20]. Lei Yang *et al.* have reported the formation MoS_{2(1-x)}Se_{2x} alloys using CVD, where x is varied from 0 to 1 depending on the amount of S and Se in the CVD chamber.^[24] Their

studies showed that fractional values of x show improved catalytic activity compared to integral x . The comparison of their HER activity with that of pristine samples ($\text{MoS}_2/\text{MoSe}_2$) showed that the enhanced activity contribution is predominantly coming from the basal plane of the alloys. Hence, it can be concluded that the HER activity of TMDs can be improved by making alloys as well as engineering the edges in the structure. In the similar direction, Feng *et. al* reported a physical vapor deposition method for morphologically controlled Mo-zigzag and S/Se zigzag edged oriented single layer crystals by tuning the growth temperature and temperature gradient in the quartz tube.^[13] But the morphologies reported by Feng *et al.* were straight edged triangles, hexagons, and triangles with inward curving edges. A generalized method for the growth of morphology controlled different TMDs structures is still lacking and here we are proposing a protocol for the growth of several microns (area) sized triangle and dendritic structures of TMDs and their alloys.

Atomically thin, triangle structured MoS_2 , MoSe_2 , and $\text{MoS}_{2(1-x)}\text{Se}_{2x}$ were grown over 300 nm thick oxidized Si wafers (Si/ SiO_2). A customized two zone furnace based CVD set up was used for the growth, as shown in figure 1. Ar/H_2 (10% H_2) gas was used as the carrier gas and also providing an inert atmosphere. The flow rate was kept as 200 sccm during the entire growth process. The chalcogen S and Se powders were placed in the lower temperature zone with the temperature of 200 °C and 350 °C for MoS_2 and MoSe_2 , respectively. 6 mg of MoO_3 powder in an alumina crucible and the SiO_2/Si wafer suspended over it were kept in the high temperature zone (as shown in figure 1) with a temperature of 650 °C and 750 °C for MoS_2 and MoSe_2 , respectively. The times taken for zone-II to reach 750 °C (for MoSe_2 or 650 °C for MoS_2) and zone-I to reach 350 °C (for Se or 200 °C for sulfur) were kept as 25 minutes. The growth time was kept as 20 minutes for all the triangle systems. For alloys (triangle), Se was

placed at 350 °C and S was placed at the corner of lower temperature zone-I (same side) where the temperature was optimized to be 200 °C. The high temperature zone was set as 720 °C where the MoO₃ - SiO₂/Si substrate system was placed as mentioned before. The growth time was kept as 20 minute for the alloys too. In all cases, the furnace was suddenly opened after 20 minutes to arrest the growth of TMDs by sudden cooling.

For the growth of dendrites, the respective growth temperatures were kept the same as above (650 °C for MoS₂, 750 °C for MoSe₂, and 720 °C for alloys) while the growth time and the flow rates were changed. In this method, the flow of Ar/H₂ was carried out from both the sides during the growth, as shown in the figure 1a & 1b. A higher flow rate of 350 sccm was kept during the growth of dendritic structures and the entire growth time was kept as 9 minutes. The precursor arrangement for MoS₂/MoSe₂ dendrite was kept exactly the same as that of triangle growth while a higher flow rate was kept as mentioned before. After the growth of initial 6 minutes, the direction of Ar/H₂ flow (indicated by red arrows) was reverted immediately to the opposite direction (green arrows) for the next two minutes. The growth was then arrested by the sudden cooling of the furnace. For the alloy dendrite growth, the precursors were kept in the same manner as for the triangled alloy structures, while the flow rate and the direction were tuned as mentioned for MoS₂/MoSe₂ dendritic growth.

The as grown TMDs were transferred from the SiO₂/Si substrate to glassy carbon (GC, 3 mm diameter) electrodes using a polymer assisted transfer technique. In this method, the CVD grown TMD/SiO₂/Si substrate was spin-coated with polymethyl methacrylate (PMMA) and then kept for drying. The PMMA coated TMDs/SiO₂/Si substrate was dipped in 2 M KOH solution for one day to etch away the SiO₂ layer. This will result the separation of PMMA/TMDs from the Si substrate (the Si substrate will then sink in the KOH solution container while the

PMMA/TMDs film will float on the top). PMMA/TMDs was further scooped out using the GC electrode. The scooped out PMMA/TMDs thin film on GC electrode was thoroughly washed in triple distilled water to remove the KOH. The GC electrode was then left to air dry and the PMMA was washed off with acetone and isopropanol, successively. These GC/TMDs systems were used as working electrode in the electrochemical HER measurements (see method section for the details of electrochemical set up).

Water bubblers are connected *via* exhaust tubes to both ends of the tubular chamber to trap the toxic by-products formed during the reaction. In order to achieve the dendritic structures low vapour pressure of Mo/S is required ^[22]. This has been achieved by a simple modification of the conventional CVD based TMD growth technique, as shown in the schematic figure 1a. The time-temperature/flow rate profile for the dendrite growth is shown in figure 1b. The opposite flow is indicated by the negative flow rate values in the profile. The suddenly changed opposite direction of the Ar/H₂ gas flow will lead to the low Mo/S vapour pressure and thus it is hypothesized to form dendritic structures. In general, single layer TMDs are formed in a triangular fashion, which is thermodynamically favourable, while an immediate change in the gas flow direction will result in a growth mode that is kinetically favoured.

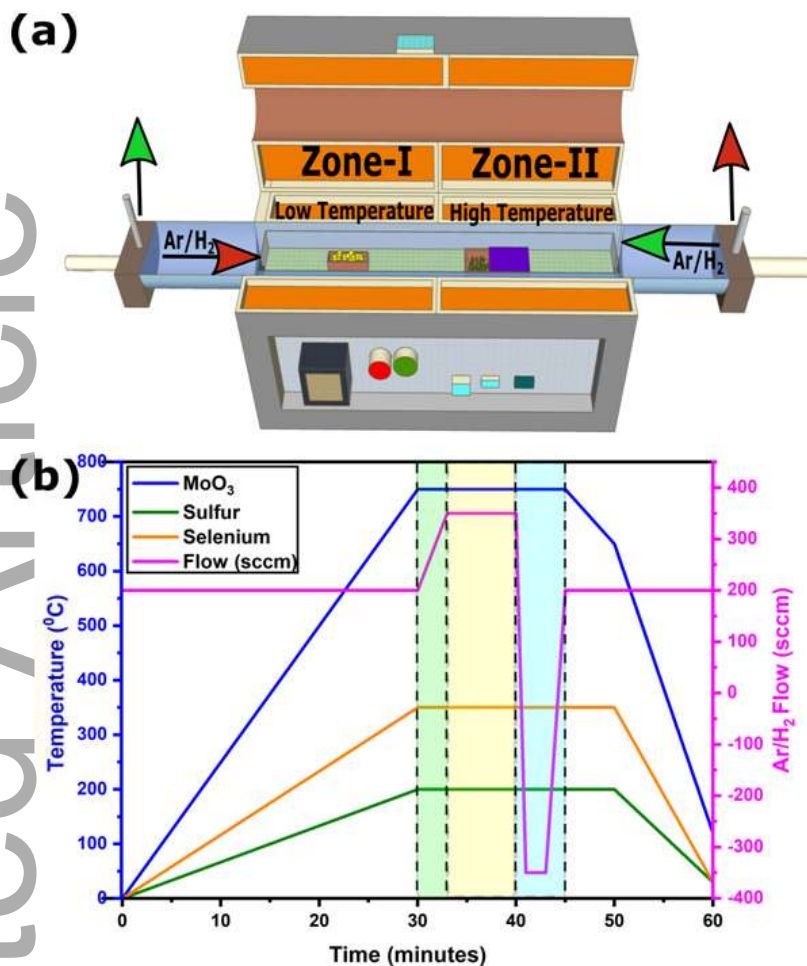


Figure 1. a) In house developed CVD setup for dendritic growth of TMDs. The arrows represent the Ar/H₂ flow and its exit in each directions. b) Time-temperature profile for the growth of dendrites. Note that the negative flow rate of Ar/H₂ indicates opposite direction of Ar/H₂ flow.

Figure 2 (a-c) shows optical images of the resultant MoS₂, MoSe₂, and MoS_{2(1-x)}Se_{2x}, with triangular shaped grains whereas figure (d-f) represents the corresponding dendritic morphology structures. Figure 2(g-i) shows scanning electron microscope (SEM) images of MoS₂, MoSe₂, and MoS_{2(1-x)}Se_{2x} dendrites, respectively. The optical images show that these dendrites are uniformly monolayer (by optical contrast) with a large number of edge sites. From the SEM analyses, lateral size of the triangles and dendrites of the TMDs are found to be ~ 30-

100 μm . The large area coverage and uniform growth are further verified by low resolution optical and SEM images, as shown in the supporting information, figure S1 and S2 respectively.

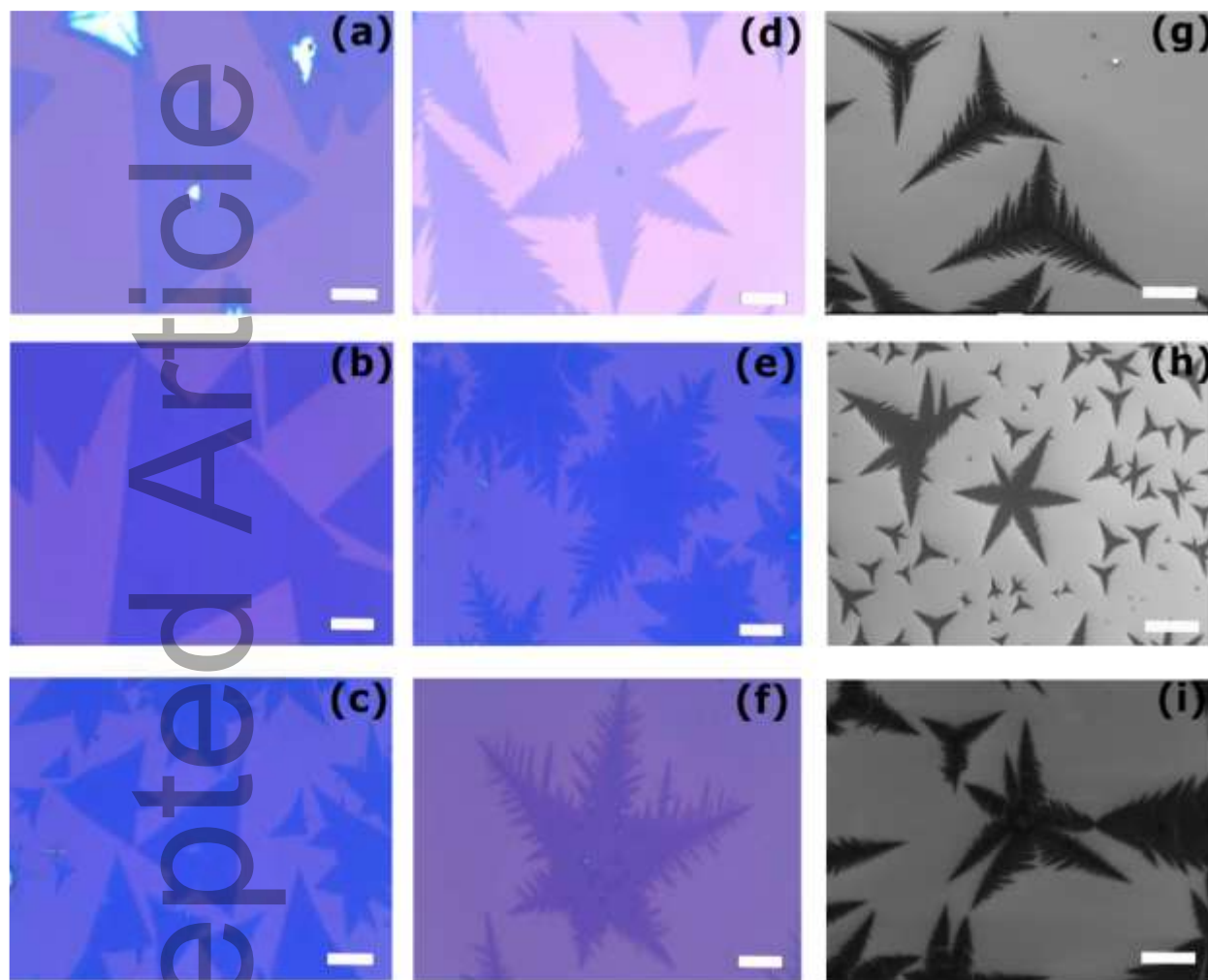


Figure 2: Optical microscope images of triangular morphology of (a) MoS_2 (b) MoSe_2 and (c) $\text{MoS}_{2(1-x)}\text{Se}_{2x}$ and dendritic Morphology of (d) MoS_2 (e) MoSe_2 and (f) $\text{MoS}_{2(1-x)}\text{Se}_{2x}$. SEM images of (g) MoS_2 , (h) MoSe_2 (i) $\text{MoS}_{2(1-x)}\text{Se}_{2x}$ dendrites. All scale bars are 20 μm .

The crystalline quality and alloying of the TMD structures are confirmed using micro Raman spectroscopy and mapping. Figure 3a shows the comparison of Raman spectra from triangular and dendritic MoS_2 , MoSe_2 , and $\text{MoS}_{2(1-x)}\text{Se}_{2x}$. TMDs show significant and

dominating Raman peaks originating from the in-plane (E_{2g}) and out of plane (A_{1g}) vibration modes of chalcogens.^[25] It is found that there are no significant changes in peak position and line widths of the Raman modes from dendrite to triangle structures of the same alloy composition. The separation between the E_{2g} and A_{1g} vibrational modes is very sensitive to the number of layers of a particular TMD. In the case of MoS_2 and MoSe_2 , the separations between these two vibration modes are found to be ~ 20 and $\sim 46 \text{ cm}^{-1}$, respectively, indicating the presence of respective single layers.^[26]

The $\text{MoS}_{2(1-x)}\text{Se}_{2x}$ alloy has four dominating peaks of which two are the E_{2g} and A_{1g} peaks from S--Mo--S bonds at 368 cm^{-1} and 398 cm^{-1} , respectively. The other two peaks at 217 cm^{-1} and 264 cm^{-1} are due to vibrations from partially selenized MoS_2 (S--Mo--Se).^[27] Even though the alloy structures are found to be single monolayers, the separation between E_{2g} and A_{1g} modes of MoS_2 is around 30 cm^{-1} due to strain induced effects in the lattice *via* Se doping. Hence, the Raman studies confirm the formation of alloys, both in dendritic and triangle shaped structures.

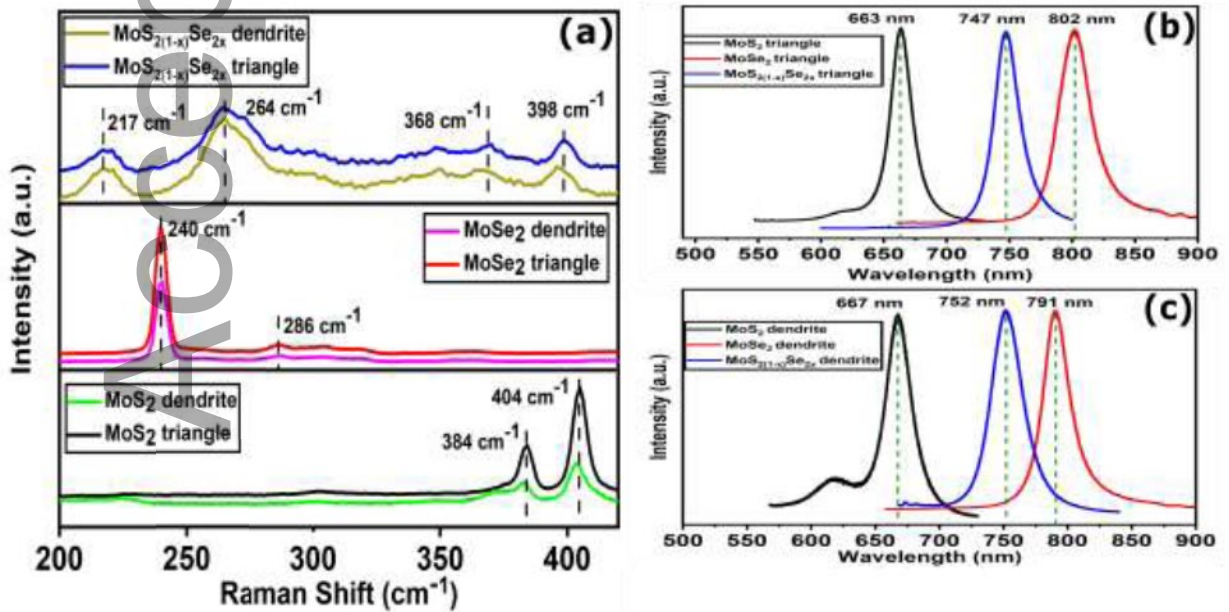


Figure 3: a) The micro-Raman spectra of MoS₂, MoSe₂, and MoS_{2(1-x)}Se_{2x} triangular and dendrite structures (532 nm laser excitation for all). Photoluminescence (PL) from MoS₂, MoSe₂, and MoS_{2(1-x)}Se_{2x} (b) triangular, and (c) dendritic structures. (633 nm laser (excitation) was used for MoSe₂ and MoS_{2(1-x)}Se_{2x} PL and 532 nm for MoS₂ PL).

One of the important features of atomically thin TMDs, which makes them invaluable materials for optoelectronic materials, is their high photoluminescence (PL) due to the conversion of indirect bandgap to direct one while limiting the number of layers to one monolayer.^[28] It is found that MoS₂, MoSe₂, and MoS_{2(1-x)}Se_{2x} show PL at 663, 802 and 747 nm respectively, which shows that these alloys have great potential in the band gap tunability of TMDs. The PL from the MoS₂ has two clear peaks A (dominating one) and B (small peak), correspond to direct band transitions at the K point of Brillouin zone.^[29] Two peaks come from the valence band splitting in monolayer TMDs due to the presence of strong spin-orbit coupling. The difference between these two peaks (A and B) yields a valence band splitting of ~ 0.2 eV^[29] and 0.25 eV^[30] for MoS₂ and MoSe₂, respectively. The PL mapping is carried out on the dendritic structures (supplementary information, figure S3) indicating the uniformity of these structures at a micrometer scale.

In order to further estimate the presence of 'Se' and the local environment of chemical composition in pristine MoS₂ and MoS_{2(1-x)}Se_{2x} alloys, X-ray photoelectron spectroscopy (XPS) measurements were performed. Figure 4 shows the core level XPS bands of Mo-3d, S-2p, Se-3d, and O-1s in MoS₂ and MoS_{2(1-x)}Se_{2x}. A XPS survey spectrum and the corresponding peak positions and their binding energies are shown in the supporting information (figure S4), indicating the presence of Mo, S, Se, and O. Figure 4a shows the comparison of Mo-3d core level XPS spectra in MoS₂ and MoS_{2(1-x)}Se_{2x}, respectively. As shown in figure 4a, the strongest

Mo-3d doublet peaks for $[\text{MoS}_2]$ and $[\text{MoS}_{2(1-x)}\text{Se}_{2x}]$ are detected at $[230.0 \text{ eV } (3d_{5/2}) \text{ \& } 233.1 \text{ eV } (3d_{3/2})]$, and $[229.6 \text{ eV \& } 232.8 \text{ eV}]$, respectively corresponding to the 4+ oxidation state. The characteristic peaks corresponding to S $2p_{3/2}$ and S $2p_{1/2}$ orbitals of the divalent sulphide ions (S^{2-}) in $[\text{MoS}_2]$ and $[\text{MoS}_{2(1-x)}\text{Se}_{2x}]$ are located at $[162.8 \text{ eV \& } 164.0 \text{ eV}]$ and $[162.5 \text{ eV \& } 163.7 \text{ eV}]$, respectively. Besides, an additional peak is observed at 161.2 eV, which may be due to the formation of S-Se and amorphous sulphur in the $\text{MoS}_{2(1-x)}\text{Se}_{2x}$ system.^[31] Interestingly, the observed negative binding energy shifts in both Mo-3d ($3d_{5/2}$, $3d_{3/2}$) and S-2p ($2p_{3/2}$, $2p_{1/2}$) around 0.3 eV in $\text{MoS}_{2(1-x)}\text{Se}_{2x}$ with respect to MoS_2 can be due to the alloying of 'Se' with MoS_2 basal plane lattice (which is later proven using TEM). It is well known that when a less electronegative element is added to the system there will be negative binding energy shift.^[32] Since Se is less electronegative than S, the shift in XPS can be attributed to the alloying. In particular, the formation of $\text{MoS}_{2(1-x)}\text{Se}_{2x}$ is identified by Se-3d, which exhibits two doublet peaks $3d_{5/2}$, $3d_{3/2}$ detected at 54.9 eV, 55.8 eV, respectively, as shown in figure 4c. The percentage (atomic%) of Se on MoS_2 is found to be ~34%, indicating that x is 0.34. Figure 4d displays the O-1s spectra from the MoS_2 and $\text{MoS}_{2(1-x)}\text{Se}_{2x}$ samples. The O-1s spectrum of MoS_2 is peaked at 529.3 eV whereas that in $\text{MoS}_{2(1-x)}\text{Se}_{2x}$ alloy is peaked at 529.5 eV. The relative intensities of the O-1s spectra in the MoS_2 and $\text{MoS}_{2(1-x)}\text{Se}_{2x}$ samples are almost identical. The nature of the spectra show that the presence of oxygen might be due to the formation of physisorbed oxygen during the atmospheric CVD growth process.

The Se distribution over the MoS_2 basal plane is further estimated from high angle annular dark field (HAADF) - scanning transmission electron microscope (STEM), operating at 80 kV, as shown in figure 4(e-f). Figure 4(e) shows the HAADF-STEM images of pristine monolayer MoS_2 and that of $\text{MoS}_{2(1-x)}\text{Se}_{2x}$ alloy is shown in figure 4(f). The bright spots

correspond to Mo sites and columns are filled with S atoms in case of MoS₂ as shown in figure 4e. It is to be noted that the HAADF intensity of S atoms is rather low, which may be due to the marginal contamination from PMMA residue during the electron beam exposure. It is very important to understand the Se distribution in the MoS₂ layers as it affects the structure's properties. For example, a material in which subsequent atomic layers have different dopant concentrations will have different properties from the one consisting of identical alloy layers.^[33] Atomic scale chemical analysis using HAADF-STEM imaging is more challenging for thicker samples than monolayers due to the overlapping of atoms in the different layers.^[34] An example of consecutive mono and bi layer AB stacked Se doped MoS₂ is shown in the supporting information in figure S5(a-b), which shows that a drastic variation of image contrast (see dark and bright field STEM image) can be observed at the atomic sites which makes visual interpretation in stacked layers challenging. Note that the HAADF-STEM imaging is performed on several locations of the monolayer MoS_{2(1-x)Se_{2x}} sample to estimate Se doping as shown in the supporting information figure S6. HAADF-STEM imaging clearly shows the formation of atomically thin crystalline layers.

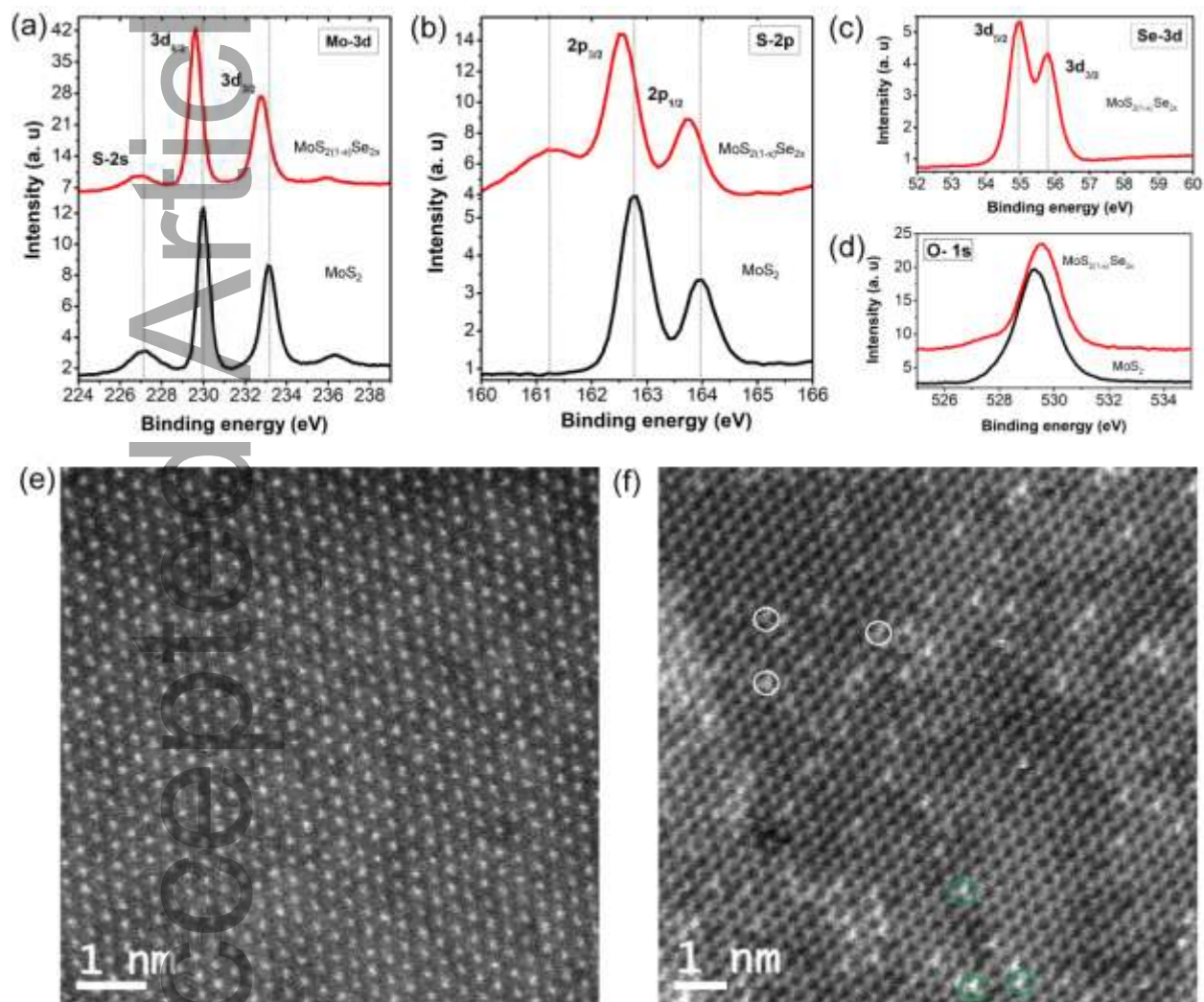


Figure 4: XPS core level spectra for (a) Mo-3d, (b) S-2p in pristine MoS₂ and MoS_{2(1-x)Se_{2x}} alloys, (c) Se 3d in MoS_{2(1-x)Se_{2x}}. (d) O-1s core level XPS spectra of MoS₂ and MoS_{2(1-x)Se_{2x}}. HAADF-STEM images of a monolayer (e) MoS₂ and (f) MoS_{2(1-x)Se_{2x}}. Note that the white and green circles denote the Se+S and Se₂ atomic sites, respectively.

Gong *et al.* reported the quantitative site-separated histogram analysis for Se distribution in mono and bilayer MoS₂ using HAADF-STEM image intensity from atomic arrangement of Mo, S₂, Se+S, and Se₂ sites.^[33] Based on their analysis, Mo atoms display brighter intensity than the S₂ sites in pristine MoS₂ hexagonal lattice while in the case of Se doped MoS₂ some S₂ sites become much brighter and display intensities close to or even higher than the Mo sites with the intensities of the Mo sites remaining unchanged. They quantitatively evaluated that higher image intensity at the S₂ sites arises from Se substitution (Se+S) and Se₂, which are brighter than Mo.^[33] Interestingly, we have found similar observations from our HAADF-STEM image analysis as shown in figure 4 (e-f), in which S₂ is substituted with single Se (Se+S) highlighted with white rings and double sites (Se₂) are highlighted with green rings (see figure 4(e)).

In order to assess the impact of structural (morphological) variations on the inherent electrocatalytic hydrogen evolution reaction (HER) properties of these TMDs, the CVD grown monolayer triangular as well as dendritic structures of MoS₂, MoSe₂, and MoS_{2(1-x)}Se_{2x} were first transferred as such onto GC electrodes (as mentioned before). For instance, figure S7 shows the optical and SEM images of transferred dendritic MoS_{2(1-x)}Se_{2x} structure from SiO₂/Si substrate to GC electrode along with their Raman and PL spectra. Remarkably, the shapes of the dendritic structure seem nearly intact before to (figure S7a and b) and after the transfer (figure S7c and d) process, suggested the perfect preservation of the edge sites. Similarly, the Raman (figure S7e) and PL ((figure S7f) spectra of transferred MoS_{2(1-x)}Se_{2x} flakes on GC are matching well with that of monolayer MoS_{2(1-x)}Se_{2x} as grown on SiO₂/Si. The red shift in A excitonic peak in PL spectra before and after the transfer process can be attributed to the released interfacial strain effect during wet transfer procedure or changes in the dielectric environment. The TMDs transferred onto GC electrodes were further systematically explored for HER studies using linear

scan voltammetry (LSVs) (details in experimental section) using a three electrode system with graphite rod (Pt counter electrode is also checked and got similar results) as counter electrode. It is to be noted that the LSV polarisation curves presented here are not iR compensated, since it is known that uncompensated data will be more meaningful while comparing the activity of two different materials at the same current density using the similar electrochemical set up.^[35]

The HER polarization curves were taken in 0.5 M H₂SO₄ at a scan rate of 2 mV s⁻¹ revealing the respective HER performances, as depicted in figure 5a. The current densities were normalized by the electrochemical active surface area (calculated using Randles-Sevcik equation, details in supporting information). The HER performances of the bare GC and benchmarked commercially available Pt/C catalyst are also performed comparably. As observed (figure 5a), the TMDs modified GC electrodes are HER active, presenting less onset overpotential (η_0) and high current densities in compare to bare GC. Among the TMDs, the monolayer triangle MoS₂ exhibits a poor HER activity (high η_0), whereas the monolayer dendritic MoS_{2(1-x)}Se_{2x} alloy exhibits the highest HER activity and have the lowest onset overpotential and high current densities than others. The variations of onset overpotential (η_0) and overpotential at current density 10 mA cm⁻² (η_{10}) of all electrodes are summarized in the figure 5b. It is also worth noting that the triangular shaped monolayer TMD flakes are less HER active than the respective dendritic structures. To achieve a current density of 10 mA cm⁻² (a benchmarked value while comparing the solar to hydrogen conversion), the triangle shaped MoS₂, MoSe₂ and MoS_{2(1-x)}Se_{2x} require overpotentials of 540, 485 and 349 mV, respectively whereas for the same current density, the dendritic structure of MoS₂, MoSe₂, and MoS_{2(1-x)}Se_{2x} require overpotentials of only 394, 326 and 241 mV, respectively. As observed, the η_{10} shifts positively when structure of TMD flakes changes from triangular to dendritic structure, which is

expected due to fact that the electrocatalytic activities of TMDs are strongly related to it exposed edge sites.^[22-23] It has been well reported theoretically as well as experimentally that edge sites of 2D TMDs are catalytic active for HER due to their low hydrogen binding energy (ΔG_H) whereas the basal planes are catalytically inert.^[20] Additionally, it has been also reported that the ternary TMD alloys exhibits better HER performance than that of their binary counterparts due to presence of different radii of atoms on the basal planes which can induced the lattice distortion and can create many more unsaturated active sites.^[36] Thus, lattice distortion in $\text{MoS}_{2(1-x)}\text{Se}_{2x}$ alloy may further leads the active basal planes too along with its active edge site. Therefore, the high activity of $\text{MoS}_{2(1-x)}\text{Se}_{2x}$ dendritic structure can be ascribed due to the synergic effects of abundant catalytic active edge sites as well as their active basal plane. Furthermore, in order to confirm the inherent HER activity of TMDs is not due to other artefacts, the current densities are also calculated using the geometric surface area of the electrode (supporting information figure S8), where it also shows a similar trend of HER activity as that shown in figure 5a. All these measurements are carried out using graphite counter electrode and the HER activity of benchmarked Pt/C is also shown in figure 5a. The comparison of LSV polarization curves of different TMD structures with current density calculated using both electrochemical surface area and geometrical area are given in figure S9 (the x-axis scaling is same for all the curves). The enhanced HER activity (decrease in over potential and increase in current density) while moving from triangle to dendrite is evident in both MoS_2 and MoSe_2 , indicating the enhanced activity due to edges. Further, the activity of $\text{MoS}_{2(1-x)}\text{Se}_{2x}$ triangle is much higher than that of MoS_2 triangle and dendrite, indicting the activity enhancement due to basal plane Se doping (which is proven *via* STEM analyses). Moreover, the activity of $\text{MoS}_{2(1-x)}\text{Se}_{2x}$ triangle is further enhanced

when the morphology was changed from triangle to dendrite (figure S9F), indicating the role of edges in this basal plane Se doped MoS₂ dendrite.

Further, to evaluate the efficiency of the catalysts, Tafel slope values were extracted from the respective Tafel plots (figure 5c). The dendritic MoS₂(1-x)Se_{2x} structure showed the lowest Tafel slope (67 mV/dec) than those of triangle shape MoS₂ (164 mV/dec), MoSe₂ (148 mV/dec), and MoS₂(1-x)Se_{2x} (101 mV /dec) triangle flakes as well as dendritic structures of MoS₂ (122 mV/dec) and MoSe₂ (91 mV/dec) indicating its excellent kinetics behaviour among all. The Tafel slope of pristine MoS₂ is observed to be 164 mV/dec which is in tune with that reported for CVD grown MoS₂.^[37] A significant enhancement in HER activity was observed for MoS₂ dendrite where the Tafel slopes show a significant decrease of ~25%. Similar trend was observed in case of MoSe₂ and MoS₂(1-x)Se_{2x} too, which is tabulated in table 1. This indicates the edge induced activity changes in TMDs. Secondly, while doing the Tafel analyses on doped TMDs, it is observed a further enhancement in activity because of doping (decrease in Tafel slope), as shown in table 2. This indicates the augmented HER kinetics due to the doping.

Table 1. Comparison of Tafel slopes of triangles and dendrites.

	Tafel slope (mV/dec)		% change
MoS₂	Triangle	164	~ 25 %
	Dendrite	122	
MoSe₂	Triangle	148	~ 38 %
	Dendrite	91	
MoS₂(1-x)Se_{2x}	Triangle	105	~ 36 %
	Dendrite	67	

Table 2. Comparison of Tafel slopes of undoped and doped (alloy) TMDs..

		Alloying	Tafel Slope change (%)
Triangle	MoS ₂	MoS _{2(1-x)} Se _{2x}	~ 36 %
	MoSe ₂		~ 29 %
Dendrite	MoS ₂	MoS _{2(1-x)} Se _{2x}	~ 45 %
	MoSe ₂		~ 26 %

To further confirm the observed HER activity trends of TMDs, electrochemical impedance spectroscopy (EIS) studies were performed in HER conditions at an overpotential of 250 mV, and the results are shown in figure 5d. The charge transfer resistance (R_{ct}) values across the electrode-electrolyte interface observed after fitting Randles plot, for triangle shape MoS₂, MoSe₂ and MoS_{2(1-x)}Se_{2x}, were found to be 10.1, 6.9 and 1.6 K Ω , respectively whereas that for the dendritic structures of MoS₂, MoSe₂ and MoS_{2(1-x)}Se_{2x} are found to be 4.1, 1.1 and 0.4 K Ω , respectively. The lowest R_{ct} value of dendritic MoS_{2(1-x)}Se_{2x} alloy among all the other TMD structures indicates the augmented electron transfer kinetics of this structure, in tune with the LSV studies. The EIS curves of MoS₂, MoSe₂, and MoS_{2(1-x)}Se_{2x} triangles and dendrites are compared in figure S10, and it is clear that dendritic structures have low R_{ct} values than the corresponding triangles while doped structures have the lowest R_{ct} values in comparison to the undoped structures. These studies show that the HER activity can be tuned both by morphology control (with larger number of edges) and basal plane doping.

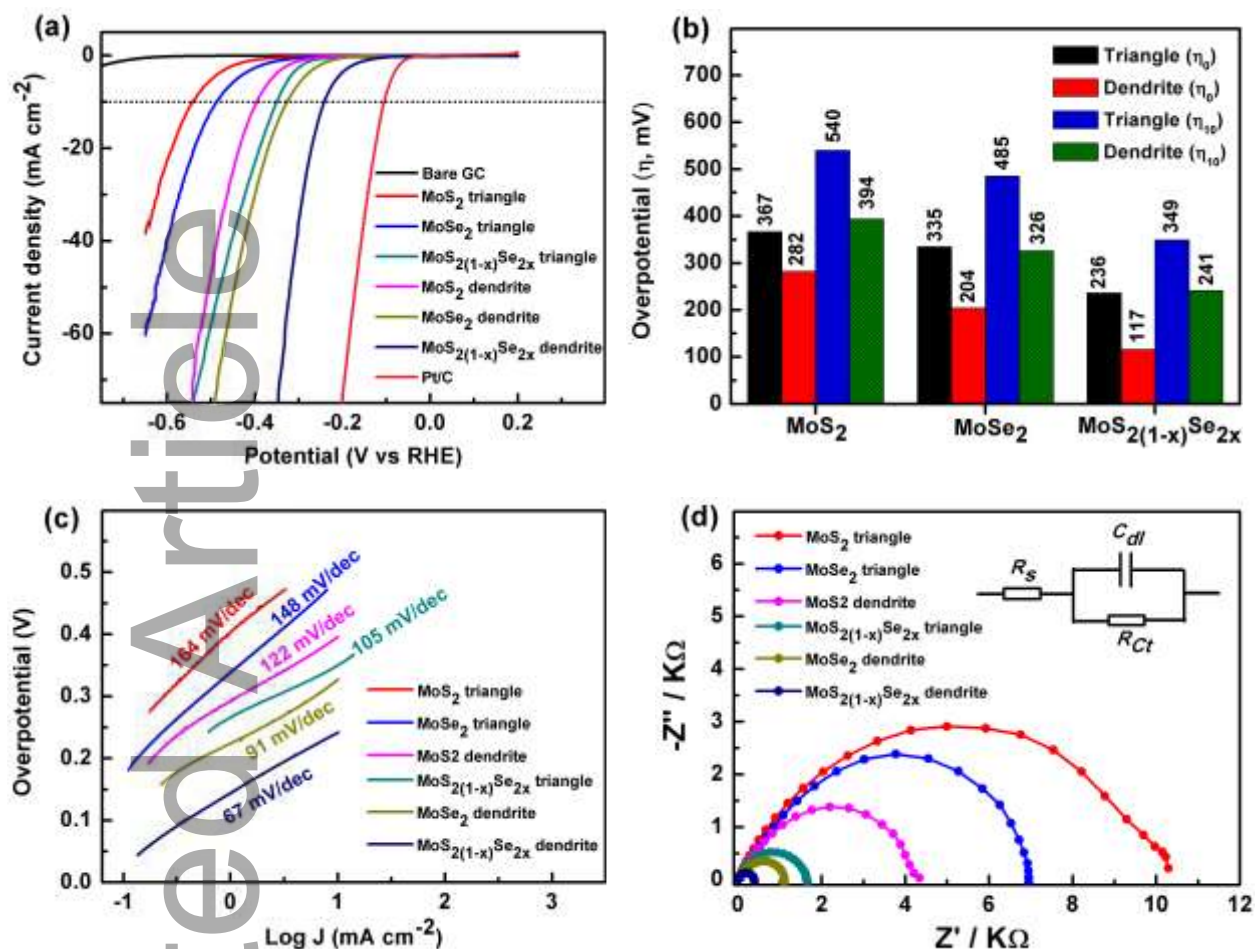


Figure 5: HER activities of triangular and dendritic shape binary and ternary TMDs on glassy carbon electrode (a) LSV curves measured in 0.5 M H_2SO_4 at scan rate of 2 mV s^{-1} . (b) Variation of onset overpotential and overpotential at 10 mA cm^{-2} . (c) Tafel plots extracted from the corresponding polarization curves. (d) Nyquist plot carried out at overpotential of 250 mV (vs. RHE) with an inset of best fitted electrical equivalent (Randles) circuit. All the measurements were carried out with graphite rod as counter electrode.

Apart from the HER activity, the operational durability of an electrocatalyst is another vital aspect to realize its capability for the long term performance. To this purpose, the stability of an optimum ternary dendritic $\text{MoS}_{2(1-x)}\text{Se}_{2x}$ electrocatalyst was tested by chronoamperometry

and the LSVs in 0.5 M H₂SO₄. Figure 6a shows the chronoamperometry response of the dendritic MoS_{2(1-x)}Se_{2x} electrocatalyst performed at an overpotential of 250 mV. The observed chronoamperometric current response of the dendritic MoS_{2(1-x)}Se_{2x} electrocatalyst is nearly constant even after more than 20,000 seconds of continuous operation indicating its high electrocatalytic stability for the long term HER performance in acidic condition. Furthermore, the electrochemical cycling stability of the dendritic MoS_{2(1-x)}Se_{2x} is also tested by measuring the polarization curves before and after 1000 cyclic voltammetry (CV) runs (figure 6b). After 1000 CVs, the dendritic MoS_{2(1-x)}Se_{2x} exhibits the reproducible HER polarization curve (only 14 mV difference in overpotential at 10 mA cm⁻²), indicating their high stability towards HER performance. A small increment in the current density was observed in the initial part of the chronoamperometry test (figure 6a), similar to that observed by Xu *et al.*,^[22] where it can be due to the presence of sulfur vacancies and their possible aggregation during the initial electrochemical process.

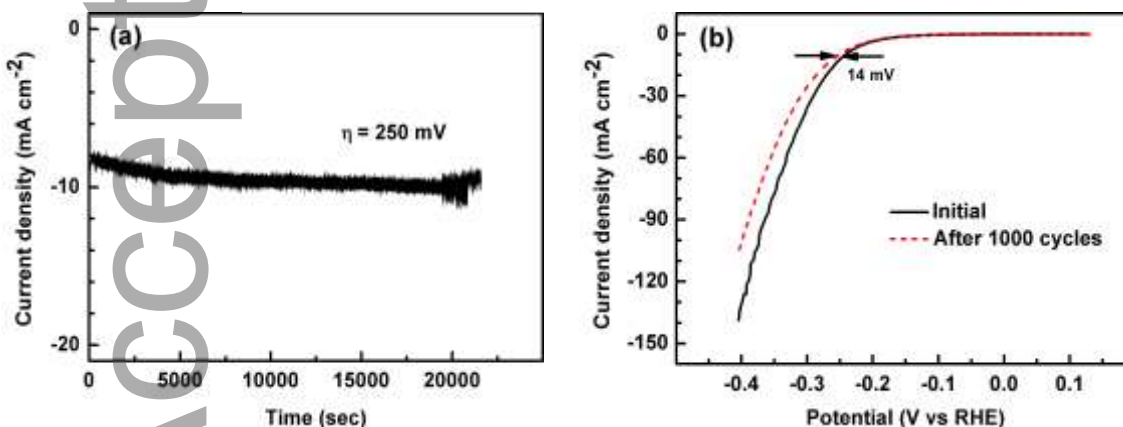


Figure 6: Stability test for dendritic MoS_{2(1-x)}Se_{2x} alloy catalyst (a) current-time response at an applied potential of -0.250 V (vs. RHE) and (b) LSV curves taken before and after 1000 voltammetry cycles at a scan rate of 2 mV s⁻¹.

Different methods are adopted to enhance the inherent HER activity of 2H-MoS₂ (which is thermodynamically more stable than its structural polymorph 1T MoS₂).^[38] But, the 2H phase shows semiconducting nature while the 1T phase has a metallic nature.^[38-39] Further, it is reported that 1T-MoS₂ has higher hydrophilicity which eventually directs the maximum interaction with the electrolyte.^[40] Furthermore, unlike in 2H-MoS₂, the basal plane of 1T-MoS₂ is also HER active.^[38] Apart from the enhanced HER activity of 1T-MoS₂ atomically thin layers (inherent activity), recently nanostructured (enhanced active sites) 1T-MoS₂ flowers were shown for their HER properties.^[38] The overpotential required for 10 mA/cm² current density (η_{10}) was reported for this structures is found to be 252 mV, which is higher than that of present 2H-MoS_{2(1-x)}Se_{2x} structures (241 mV). Further, the performance of MoS_{2(1-x)}Se_{2x} dendrite is compared with the other recent reports on CVD grown TMDs on different substrates, and the comparison is shown in table S2. This indicates that within the spectrum of thermodynamically stable TMD structures itself one can tune the HER activity of a parent crystal by controlling morphology and dopants, and this opens plethora of opportunities for engineered TMD structures for catalysis and other opto-electronic applications.

In conclusion, a novel method is proposed for the morphology controlled TMD structures of MoS₂ and MoSe₂. Atomically thin several micrometer sized triangle and dendritic MoS₂ and MoSe₂ are developed by this generalized CVD protocol, and similar morphology controlled structures of their alloy, namely 2H-MoS_{2(1-x)}Se_{2x}, are also synthesized, where the XPS analyses show that x is 0.34. Apart from the extensive HAADF-STEM based analyses, crystallinity and ultra-thinness (monolayer, ~0.83 nm) of the 2H-MoS_{2(1-x)}Se_{2x} are also proven using X-ray diffraction (XRD, figure S11) and atomic force microscopy (AFM, figure S12) studies. The doping and alloying of Se in MoS₂ are proven *via* different techniques and the possibility of

tuning the bandgap by alloying is demonstrated. HER properties of these structures in acidic medium are studied and the role of morphology in the HER performance is unravelled. The HER activities (in terms of both overpotential and Tafel slope) of triangle shaped 2H-MoS₂ and MoSe₂ are found to be augmented by changing their morphology to dendritic, and further enhancement in the HER activity can be achieved by doping 2H-MoS₂ with Se using the same synthesis set up. The 'best' HER activity is observed for the 2H-MoS_{2(1-x)}Se_{2x} dendritic structure where it is found to be even better than the recently reported nanostructured (flower shaped) inherently more active 1T-MoS₂ structures.^[38] This synthesis strategy opens intriguing opportunities for the growth of morphology controlled large area complex structures of TMDs *via* non-equilibrium CVD, with the potential of yielding structures with enhanced catalytic and tuneable optoelectronic properties, as demonstrated here.

Experimental methods:

Materials:

Molybdenum (VI) tri oxide (MoO₃, 99.95%) from SRL, sulfur (S, 99.98%) and selenium (Se, 99.99%) were purchased from sigma Aldrich.

Characterization:

Crystallinity and quality of pristine and dendritic MoS₂, MoSe₂ and MoS_{2(1-x)}Se_{2x} were studied by XRD (Cu K α radiation, λ =1.5418 Å) and micro-Raman spectroscopy (using InVia Raman spectrometer equipped with 532 and 633 nm laser excitation wavelengths) studies. The samples were focused with 100x objective lens at a laser power ~ 1 mw. The SEM images were taken using JEOL JSM7200F SEM. XPS was performed to estimate chemical composition and

atomic percentage of Se in $\text{MoS}_{2(1-x)}\text{Se}_{2x}$ alloy using KratosS5 Axis Ultra DLD spectrometer using the Al $K\alpha$ X-ray source (1486.6 eV). The HAADF-STEM studies are conducted using an aberration-corrected STEM (JEOL 2100F, 80 kV).

All the electrochemical measurements were performed in a three electrode set up using a Bio Logic SP-300 electrochemical workstation at room temperature. Transferred TMDs sample on GC electrodes were served as working electrodes, graphite rod as a counter electrode (Pt is also used to verify the data, but data is not shown), and Ag/AgCl was used as a reference electrode. The hydrogen evolution performance was carried out in 0.5 M H_2SO_4 solution using LSV technique at a scan rate of 2 mV s^{-1} . Prior to electrochemical measurements, the electrolyte was degassed by purging pure N_2 for 30 minutes. The EIS measurements were performed in the frequency ranged of 0.1 Hz to 100 KHz at an overpotential of 250 mV. All the potentials presented in this work were referenced to the reversible hydrogen electrode (RHE) using equation $E_{\text{RHE}} = E_{\text{Ag/AgCl}} + 0.197 \text{ V}$ (for 0.5 M H_2SO_4).

Acknowledgements

TNN, RS, KRS, and PKR thank Tata Institute of Fundamental Research-Hyderabad, India for the financial support. TNN acknowledges DST-SERB, India for the funding support in the form of extramural research grant for working on van der Waals solids based structures (EMR/2017/000513). PKR gratefully acknowledges DST-SERB, India for national postdoctoral fellowship (PDF/2016/001440). Authors are thankful to Mr. Mithun, at TIFR-Hyderabad for helping in AFM imaging. Authors are grateful to Dr. Balakrishna Ananthoju and Prof. Robert Dryfe, at the University of Manchester for their help in the XPS measurement. W.T and R.K.B

acknowledge the Marie-Sklodowska-Curie individual fellowship under EU H2020 Programme (H2020-MSCA-IF-2017; Grant No: 750929).

References:

- [1] Z. Lin, B. R. Carvalho, E. Kahn, R. Lv, R. Rao, H. Terrones, M. A. Pimenta, M. Terrones, *2D Mater.* **2016**, 3, 022002.
- [2] M. G. Stanford, P. D. Rack, D. Jariwala, *npj 2D Materials and Applications* **2018**, 2, 20.
- [3] T.-T. Jia, M.-M. Zheng, X.-Y. Fan, Y. Su, S.-J. Li, H.-Y. Liu, G. Chen, Y. Kawazoe, *Sci. Rep.* **2016**, 6, 18869.
- [4] Y. L. Huang, Y. Chen, W. Zhang, S. Y. Quek, C.-H. Chen, L.-J. Li, W.-T. Hsu, W.-H. Chang, Y. J. Zheng, W. Chen, A. T. S. Wee, *Nat. Commun.* **2015**, 6, 6298.
- [5] A. Kormányos, V. Zólyomi, N. D. Drummond, G. Burkard, *Phys. Rev. X* **2014**, 4, 011034.
- [6] D. Kotekar-Patil, J. Deng, S. L. Wong, C. S. Lau, K. E. J. Goh, *Appl. Phys. Lett.* **2019**, 114, 013508.
- [7] J. Kim, W. S. Yun, J. D. Lee, *J. Phys. Chem. C* **2015**, 119, 13901.
- [8] J. Ma, X. Li, L. Gan, S. Zhang, Y. Cao, Z. Nie, X. Wang, D. Ma, L. He, J. Nie, C. Xiong, R. Dou, *2D Mater.* **2018**, 5, 031015.
- [9] G. Zhang, J. Wang, Z. Wu, R. Shi, W. Ouyang, A. Amini, B. N. Chandrashekar, N. Wang, C. Cheng, *ACS Appl. Mater. Interfaces* **2017**, 9, 763.
- [10] B. Wu, D. Geng, Z. Xu, Y. Guo, L. Huang, Y. Xue, J. Chen, G. Yu, Y. Liu, *Npg Asia Materials* **2013**, 5, e36.
- [11] W. Fei, J. Yin, X. Liu, W. Guo, *Mater. Lett.* **2013**, 110, 225.
- [12] S. Wang, Y. Rong, Y. Fan, M. Pacios, H. Bhaskaran, K. He, J. H. Warner, *Chem. Mater.* **2014**, 26, 6371.
- [13] Q. Feng, N. Mao, J. Wu, H. Xu, C. Wang, J. Zhang, L. Xie, *ACS Nano* **2015**, 9, 7450.
- [14] H. Yu, M. Liao, W. Zhao, G. Liu, X. J. Zhou, Z. Wei, X. Xu, K. Liu, Z. Hu, K. Deng, S. Zhou, J.-A. Shi, L. Gu, C. Shen, T. Zhang, L. Du, L. Xie, J. Zhu, W. Chen, R. Yang, D. Shi, G. Zhang, *ACS Nano* **2017**, 11, 12001.
- [15] S. Susarla, A. Kutana, J. A. Hachtel, V. Kochat, A. Apte, R. Vajtai, J. C. Idrobo, B. I. Yakobson, C. S. Tiwary, P. M. Ajayan, *Adv. Mater.* **2017**, 29, 1702457.
- [16] J. N. Coleman, M. Lotya, A. O'Neill, S. D. Bergin, P. J. King, U. Khan, K. Young, A. Gaucher, S. De, R. J. Smith, I. V. Shvets, S. K. Arora, G. Stanton, H.-Y. Kim, K. Lee, G. T. Kim, G. S. Duesberg, T. Hallam, J. J. Boland, J. J. Wang, J. F. Donegan, J. C. Grunlan, G. Moriarty, A. Shmeliov, R. J. Nicholls, J. M. Perkins, E. M. Grievson, K. Theuwissen, D. W. McComb, P. D. Nellist, V. Nicolosi, *Science* **2011**, 331, 568.
- [17] L. Yuan, J. Ge, X. Peng, Q. Zhang, Z. Wu, Y. Jian, X. Xiong, H. Yin, J. Han, *AIP Adv.* **2016**, 6, 125201.
- [18] a) R. K. Biroju, D. Das, R. Sharma, S. Pal, L. P. L. Mawlong, K. Bhorkar, P. K. Giri, A. K. Singh, T. N. Narayanan, *ACS Energy Lett.* **2017**, 2, 1355; b) P. K. Rastogi, S. Sarkar, D. Mandler, *Appl. Mater. Today* **2017**, 8, 44.

- [19] R. Kronberg, M. Hakala, N. Holmberg, K. Laasonen, *Phys. Chem. Chem. Phys.* **2017**, *19*, 16231.
- [20] T. H. M. Lau, X. Lu, J. Kulhavy, S. Wu, L. Lu, T.-S. Wu, R. Kato, J. S. Foord, Y.-L. Soo, K. Suenaga, S. C. E. Tsang, *Chem Sci.* **2018**, *9*, 4769.
- [21] S. Pal, K. K. Tadi, P. M. Sudeep, S. Radhakrishnan, T. N. Narayanan, *Mater. Chem. Front.* **2017**, *1*, 319.
- [22] W. Xu, S. Li, S. Zhou, J. K. Lee, S. Wang, S. G. Sarwat, X. Wang, H. Bhaskaran, M. Pasta, J. H. Warner, *ACS Appl. Mater. Interfaces* **2018**, *10*, 4630.
- [23] Y. Zhang, Q. Ji, G.-F. Han, J. Ju, J. Shi, D. Ma, J. Sun, Y. Zhang, M. Li, X.-Y. Lang, Y. Zhang, Z. Liu, *ACS Nano* **2014**, *8*, 8617.
- [24] L. Yang, Q. Fu, W. Wang, J. Huang, J. Huang, J. Zhang, B. Xiang, *Nanoscale* **2015**, *7*, 10490.
- [25] R. Saito, Y. Tatsumi, S. Huang, X. Ling, M. S. Dresselhaus, *J. Phys. Condens. Matter* **2016**, *28*, 353002.
- [26] a) K. F. Mak, C. Lee, J. Hone, J. Shan, T. F. Heinz, *Phys. Rev. Lett.* **2010**, *105*, 136805; b) S. Tongay, J. Zhou, C. Ataca, K. Lo, T. S. Matthews, J. Li, J. C. Grossman, J. Wu, *Nano Lett* **2012**, *12*, 5576.
- [27] S.-H. Su, Y.-T. Hsu, Y.-H. Chang, M.-H. Chiu, C.-L. Hsu, W.-T. Hsu, W.-H. Chang, J.-H. He, L.-J. Li, *Small* **2014**, *10*, 2589.
- [28] C. Ruppert, O. B. Aslan, T. F. Heinz, *Nano Letters* **2014**, *14*, 6231.
- [29] G. Eda, H. Yamaguchi, D. Voiry, T. Fujita, M. Chen, M. Chhowalla, *Nano Lett* **2011**, *11*, 5111.
- [30] P. Tonndorf, R. Schmidt, P. Böttger, X. Zhang, J. Börner, A. Liebig, M. Albrecht, C. Kloc, O. Gordan, D. R. T. Zahn, S. Michaelis de Vasconcellos, R. Bratschitsch, *Opt. Express* **2013**, *21*, 4908.
- [31] K. K. Paul, N. Sreekanth, R. K. Biroju, T. N. Narayanan, P. K. Giri, *Sol. Energ. Mat. Sol. C.* **2018**, *185*, 364.
- [32] v. d. Heide, in *X- Ray Photoelectron Spectroscopy*, DOI: 10.1002/9781118162897.fmatter (Ed: P. v. d. Heide) **2011**.
- [33] Y. Gong, Z. Liu, A. R. Lupini, G. Shi, J. Lin, S. Najmaei, Z. Lin, A. L. Elías, A. Berkdemir, G. You, H. Terrones, M. Terrones, R. Vajtai, S. T. Pantelides, S. J. Pennycook, J. Lou, W. Zhou, P. M. Ajayan, *Nano Lett* **2014**, *14*, 442.
- [34] a) O. L. Krivanek, M. F. Chisholm, V. Nicolosi, T. J. Pennycook, G. J. Corbin, N. Dellby, M. F. Murfitt, C. S. Own, Z. S. Szilagy, M. P. Oxley, S. T. Pantelides, S. J. Pennycook, *Nature* **2010**, *464*, 571; b) W. Zhou, M. P. Oxley, A. R. Lupini, O. L. Krivanek, S. J. Pennycook, J.-C. Idrobo, *Microscopy and Microanalysis* **2012**, *18*, 1342.
- [35] S. Anantharaj, S. R. Ede, K. Karthick, S. Sam Sankar, K. Sangeetha, P. E. Karthik, S. Kundu, *Energy Environ. Sci.*, **2018**, *11*, 744.
- [36] Q. Gong, L. Cheng, C. Liu, M. Zhang, Q. Feng, H. Ye, M. Zeng, L. Xie, Z. Liu, Y. Li, *ACS Catal.* **2015**, *5*, 2213.
- [37] Z. Wang, Q. Li, H. Xu, C. Dahl-Petersen, Q. Yang, D. Cheng, D. Cao, F. Besenbacher, J. Lauritsen, S. Helveg, M. Dong, *Nano energy*, **2018**, *49*, 634-643
- [38] S. Venkateshwaran, S. M. Senthil Kumar, *ACS Sustain. Chem. Eng.* **2019**, *7*, 2008.
- [39] L. Chacko, P. K. Rastogi, P. M. Aneesh, *J. Electrochem. Soc.* **2019**, *166*, H263.

- [40] X. Geng, W. Sun, W. Wu, B. Chen, A. Al-Hilo, M. Benamara, H. Zhu, F. Watanabe, J. Cui, T.-p. Chen, *Nat Commun.* **2016**, 7, 10672.

Keyword: CVD, Transition Metal Dichalcogenide, Dendritic Structures, Hydrogen Evolution, Atomically Thin Alloys.

Rahul Sharma, Krishna Rani Sahoo, Pankaj Kumar Rastogi, Ravi K. Biroju, Wolfgang Theis, and Tharangattu N. Narayanan*

On the Synthesis of Morphology Controlled Transition Metal Dichalcogenides *via* CVD for Electrochemical Hydrogen Generation



A generalized CVD based synthesis strategy for morphology controlled TMDs and their alloys, and the enhanced hydrogen evolution activities of dendritic TMD alloys:

Optical images of dendritic 2H-MoS_{2(1-x)}Se_{2x} structures are shown in the figure with their photoluminescence properties indicated by the red colour. Augmented electro-catalytic hydrogen generation is also shown in the schematic.